Materials & Design 236 (2023) 112507

Contents lists available at ScienceDirect

Materials & Design

journal homepage: www.elsevier.com/locate/matdes

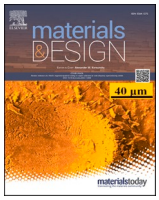

Local strength of bainitic and ferritic HSLA steel constituents understood using correlative electron microscopy and microcompression testing

R.M. Jentner [a], S. Scholl [b], K. Srivastava [b], J.P. Best [a], C. Kirchlechner [a,c], G. Dehm [a,*]

[a] Max-Planck-Institut für Eisenforschung GmbH, Max-Planck-Straße 1, 40237 Düsseldorf, Germany
[b] AG der Dillinger Hüttenwerke, Werkstraße 1, 66763 Dillingen/Saar, Germany
[c] Institute for Applied Materials, Karlsruhe Institute of Technology, 76344 Eggenstein-Leopoldshafen, Germany

ARTICLE INFO

Keywords:
HSLA-steel
Micropillar compression
Strengthening
Granular bainite
Polygonal ferrite
Dislocation density

ABSTRACT

HSLA steels with different polygonal ferrite and granular bainite contents resulting from two different cooling rates were investigated. Micropillar compression tests, electron channeling contrast imaging (ECCI) and electron backscatter diffraction (EBSD) experiments were performed to reveal microscopic strength differences and their origin. The obtained results indicate that a higher cooling rate caused a smaller granular bainite substructure size and a higher dislocation density for both ferrite and bainite. In addition, the critical resolved shear stress (CRSS) values for both phases were found to be higher for the faster cooling process. This is ascribed to the increased dislocation density for faster cooling rather than the grain size as will be discussed in the manuscript. Interestingly, the macroscopic yield strength can be closely estimated by the CRSS obtained from micropillar compression considering the corresponding phase fractions. The achieved results can be used in future as input variables for crystal plasticity models.

1. Introduction

High-strength low–alloy (HSLA) steels contain a complex microstructure. They are frequently used for pipelines or construction due to their technical and mechanical properties [1–4]. This type of steel typically consists of various types of body–centered cubic (bcc) structures (polygonal ferrite, bainite) and residual martensite-austenite as well as a carbon rich second phase (cementite or carbide precipitates) [4–7]. Previous studies frequently proved that the combination between polygonal ferrite and granular bainite eventuates in a good combination of strength and ductility [8–10]. Granular bainite is defined as a mixture of irregular ferrite with carbon rich particles distributed between the irregular ferrite grains [1,11]. Irregular ferrite is also referred to as bainitic ferrite and consists of ferrite sheaves according to high resolution transmission electron microscopy (TEM) investigations [12,13]. The sub-grains are separated by low angle boundaries [6,14]. A thin carbide or austenite film can sometimes occur depending on the chemical composition [6,14]. Steel grades with a low carbon concentration are typically associated with a bainite phase transformation with the absence of carbides, retained austenite or martensite between the sub–grains [6]. For a better separation of the two phases[1], in the following, the term granular bainite refers exclusively to the irregular ferrite. In order to adapt the mechanical properties to the desired requirements in the most cost-effective way, crystal plasticity models are becoming increasingly important to investigate the correlation between microstructure and mechanical properties of the bulk material [15–17]. The critical resolved shear stress (CRSS) of the activated slip systems is one of the main input variables for crystal plasticity models to simulate the mechanical bulk behavior. However, the investigated constituents of a HSLA steel have not been characterized regarding their micromechanical properties. Therefore, this work is dedicated to the characterization of the micromechanical properties of polygonal ferrite and granular bainite. The resulting findings can serve as input variables for crystal plasticity models that support the design the new generation of bainitic steels.

Micropillar compression is a specialized technique allowing for the CRSS of the individual constituents to be ascertained. For instance, the constituents of a dual phase (DP) steel, namely polygonal ferrite and martensite, have been characterized in terms of their CRSS and activated slip systems by previous investigations [17–19]. Through these

* Corresponding author.
E-mail address: dehm@mpie.de (G. Dehm).

[1] We are referring to the constituents “polygonal ferrite” and “granular bainite” as phases and define their phase fraction, even though they are consisting of more than one phase each.

https://doi.org/10.1016/j.matdes.2023.112507
Received 24 April 2023; Received in revised form 14 November 2023; Accepted 16 November 2023
Available online 18 November 2023

experiments, it was shown that all three possible bcc slip systems – {1 1 0}, {1 1 2} and {1 2 3} – were activated within ferrite grains at the same CRSS while pillars containing martensite islands were characterized by a uniform deformation with a much higher strength level [17,18,20]. The higher strength and the uniform deformation of martensite are both related to the hierarchical martensite substructure consisting of packets, blocks, sub–blocks and laths up to a size of several nanometers [20,21]. As a result, the experimental findings from pillar compression tests contributed to the fact that crystal plasticity models are now able to simulate the macroscopic behavior of DP steels [16,22]. Despite the fact that HSLA steels constitute approximately 12% of the world steel production [23], a valid micromechanical characterization of the contributing phases is still missing.

Since the combination between polygonal ferrite and granular bainite offers a good combination of strength and ductility, several constructions as e.g. pipelines contain these constituents [4]. It is supposed that granular bainite can only be formed during the continuous cooling process and is accompanied by the onset of a displacive transformation but the carbon atoms are still able to diffuse [8,14]. TEM investigations revealed that irregular ferrite grains are subdivided by laths or equiaxed–large grains depending on the applied cooling rate due to displacive transformation [8,24,25]. Thus, the reduced effective grain size impedes dislocation movement by sub–grain and grain boundaries [9,26,27]. Beside Hall–Petch strengthening, Taylor hardening and precipitation strengthening are considered as the other mechanisms contributing to the strength [4,8,26,28,29]. Precipitation strengthening usually depends on the volume fraction and size distribution of carbo–nitrides, since they also act as obstacles to the dislocation movement and can be explained by the Orowan–Ashby mechanism [30]. Digital image analyses on TEM images were carried out to ascertain the precipitate size distribution and volume fraction, where correlative mechanical experiments were performed and showed that the nanoparticles contributed significantly to the mechanical strength [28,29]. Beside nanoparticles, retained martensite–austenite constituents have been mentioned to contribute the mechanical strength behavior [31]. The dislocation density strengthening (Taylor hardening) is one further important mechanism having a significant impact on the properties [4,26,28,29]. Depending on the cooling rate and the formation temperature, different dislocation densities can be produced within the constituents [26]. A previous study revealed by TEM investigations that at low cooling rates more dislocation walls are flattened due to cross–slip of screw dislocations [24]. This promoted a high amount of recovered and polygonised dislocations as well as the formation of small sub-grain and grain boundaries. Consequently, the higher dislocation densities contained within the individual constituents, increases the resistance to dislocation glide on the activated slip systems.

Due to the large morphological variety and complexity of low–carbon HSLA steels [1], it still remains an open task to micromechanically characterize the complex constituents of HSLA steels. Micropillar compression is a suitable technique to measure the CRSS and the activated slip system at the meso–scale [18]. Thus, the aim of this study was to identify the microscopic strength differences and their origin caused by varying the cooling rate in two HSLA steels. The carbon rich second phase, retained martensite-austenite particles as well as carbo–nitrides were not separately tested by micromechanical experiments. In total, two bulk samples with the same chemical composition but two different cooling rates were characterized. The application of a different cooling rate resulted in a different macroscopic strength behavior which could not be explained by traditional microstructural investigations. Moreover, electron backscatter diffraction (EBSD) and electron channeling contrast imaging (ECCI) investigations were conducted to achieve detailed information about the grain and sub–grain size as well as the dislocation density of polygonal and irregular ferrite grains. It was shown that activation of dislocation slip predominantly follows Schmid's law. The CRSS values of both tested constituents were increased by using a higher cooling rate.

2. Experimental procedure

2.1. Microstructural characterization

The two investigated HSLA steel samples that subsequently identified as S1 and S2 had the same chemical composition as listed in Table 1. Both samples were industrially produced and continuously cooled by applying a lower (S1) and higher (S2) cooling rate which differed by a factor of 30% and were below 50 K/s. Each sample had the dimension of 7 × 5 × 3 mm and was ground and polished by a suspension containing 30 nm alumina particles (OPA). Besides, ECCI was conducted to reveal additional information on the substructure using a Zeiss Merlin® field emission microscope engaged with an acceleration voltage of 30 kV. Moreover, light optical microscopy (LOM) was used to exhibit the microstructural morphology by etching the OPA polished samples with a 1% Nital solution for 30 s.

2.2. Phase classification

The phase classification of individual grains was done by using manual point-to-origin measurements to quantify the orientation gradient within a grain. The applied procedure and EBSD measurement conditions will be explained in detail within Section 2.2.1. Furthermore, a classification system to automatically separate granular bainite and polygonal ferrite grains was developed by using the EBSD–KAM value and a threshold of 3° [32,33]. This procedure allowed to quickly analyze the phase fraction and the grain size of each constituent from large EBSD scans. Here, it has to be noted that the used point–to–origin measurements and the automated classification system used the same EBSD measurement conditions.

2.2.1. Point–to–origin orientation measurements

It has been shown by point–to-origin measurements that granular bainite and polygonal ferrite can be separated based on an in–grain misorientation angle [33,34]. In case it is exceeding 3°, the constituent is classified as granular bainite. This is related to the displacive phase transformation of granular bainite [14,33]. Therefore, EBSD measurements were conducted to allocate the constituent to the selected grain before a pillar was milled by focused ion beam (FIB). All specimens were cut and EBSD measurements were performed at identical depth on the bulk samples' cross section. A step size of 50 nm and an acceleration voltage of 20 kV was used for EBSD employing a Zeiss Merlin® microscope equipped with an EDAX® Hikari detector. The obtained EBSD scans were treated by a grain dilation cleanup with a tolerance angle of 5° and a minimum grain size of 3 pixels to reduce the impact of incorrectly indexed pixels; there were not more than 5% of the pixels changed. Based on previous investigations, a grain tolerance angle of 5° was applied to distinguish between sub- and grain boundaries [32]. The procedure which has been utilized to all tested grains is exemplarily illustrated at Grain–1 and Grain–2 in Fig. 1A–C. It has been observed that the position and direction of the point–to–origin orientation measurement has an impact on the classification result and that more than one measurement is required for a unique classification [32]. Thus, three point–to–origin measurements in different directions and positions were conducted to reduce the impact of strain localizations in small grain regions (Fig. 1A–B). In the case of Grain–1, all point–to–origin measurements are indicating a misorientation angle below 3°, whereas Grain–2 contains a misorientation angle above 3° (Fig. 1C). Consequently, Grain–1 and Grain–2 were classified as polygonal ferrite and granular bainite, respectively. Care was taken that the misorientation

Table 1
Chemical composition of the continuous cooled samples S1 and S2.

[wt.%]	C	Si	Mn	Cu	Ni	Nb + V + Ti	Fe
S1 and S2	0.04	0.32	1.45	≤ 0.5	≤ 0.5	≤ 0.15	*balance*

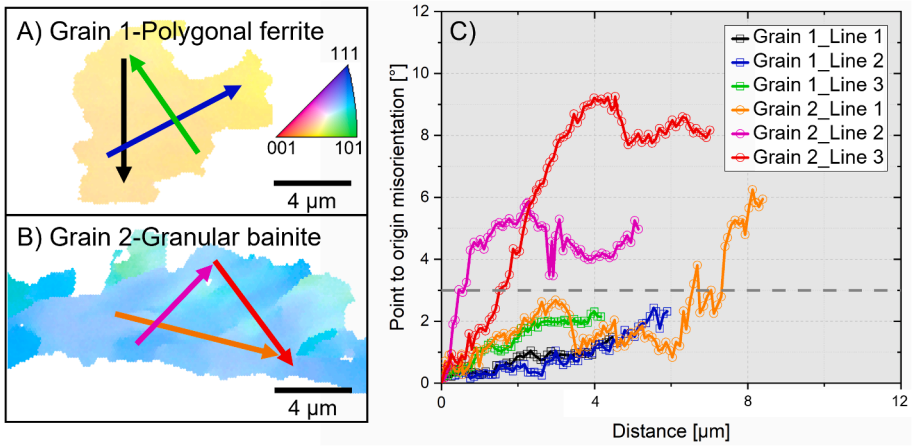

Fig. 1. Grain 1 A) and grain 2B) are two representative examples to illustrate the method how polygonal ferrite and granular bainite were distinguished. The misorientation obtained from the point–to–origin measurement within grain 1 and 2 are shown in C). Grain 1 was identified as polygonal ferrite and grain 2 as granular bainite according to the point–to–origin measurement.

gradient within each tested grain was not measured over grain boundaries since it has been shown that ferrite grains in thermomechanical processed steels may be subdivided by sub–boundaries [35].

2.2.2. EBSD–KAM classification system

After the grains were defined by selecting a grain tolerance angle of 5°, the developed classification system calculates the KAM values for each pixel and the user-defined kernel size. Comparable to the point-to-origin classification procedure, the EBSD–KAM classification also uses a 3° threshold to separate granular bainite and polygonal ferrite. Consequently, once a pixel exceeds an orientation gradient of 3°, the program assigns the related grain as granular bainite, otherwise it will be classified as polygonal ferrite. Thus, it is possible to automatically calculate the phase fraction, the grain size and orientation of each constituent and to plot a color-coded phase map. More detailed information about the classification system itself and the validation can be found elsewhere [32].

2.3. Micromechanical characterization

2.3.1. Pillar fabrication and testing

Micropillar compression tests were performed to characterize the CRSS of the activated slip system of polygonal ferrite and granular bainite grains. The retained martensite–austenite particles, as well as the carbo–nitride precipitates, were not tested by pillar compression experiments, since they were too small to be tested purposefully by this technique. Thus, to compare the constituent's CRSS, a constant pillar diameter of 2 µm was used for all experiments; all tested pillars had an aspect ratio (height/diameter) of 2 – 4 to prevent buckling instabilities during the experiment. The following criteria were relevant for using the selected diameter: (i) The selected diameter had to be smaller than the average grain size (S1: 4.7 ± 0.6 µm and S2: 4.2 ± 0.6 µm) to test the constituent without a grain boundary inside the pillar volume. (ii) The tested grain volume should be representative for the tested constituent and include strength determining features like the granular bainite substructure [8,27]. (iii) A pillar diameter below approx. 1 µm leads to an increased stochastic variation in yield stress which is related to the limited number and size of dislocations inside such small confined volumes ("size effect") [36,37]. The pillar manufacturing was done with a Zeiss Auriga® dual beam FIB with a Ga^+ ion source and a two-step milling procedure by using a current of 2 nA and finally 600 pA polishing step. This procedure allowed to achieve the best milling result considering pillar-shape and milling time. The crystallographic orientation of the single crystalline polygonal ferrite and granular bainite pillar was obtained by EBSD measurements.

A Bruker Hysitron PI88 system was installed within a Zeiss Gemini 500® field emission scanning electron microscope (SEM) to perform the *in situ* compression tests. All pillars were compressed along the transverse direction by a diamond flat punch in a displacement–controlled mode and with a strain rate of 10^{-3} s^{-1}. The *in situ* and *post mortem* observations were done with a secondary electron (SE) and in–Lense® detector using an acceleration voltage of 5 kV.

2.3.2. Pillar compression data analysis

The load and displacement data were converted to engineering stress and strain by utilizing a Mathematica® script. The calculation is based on the initial pillar height and the average pillar diameter (bottom – top pillar diameter/2). It was possible to identify the first activated slip system due to the *in situ* and *post mortem* analysis and thus to calculate the CRSS by applying $\tau_{CRSS} = m^*\sigma_{2\%}$; where m represents the Schmid factor and $\sigma_{2\%}$ the engineering stress at an engineering strain of 2%. Using the 2% engineering strain criterion reduced the impact of dislocation–dislocation interaction occurring at higher plastic strain [38]. Once the first activated slip system was identified and its CRSS calculated, the *post mortem* images were superimposed with the four slip systems whose Schmid factor was the highest. The Mathematica® script considered all three slip plane families – {1 1 0}, {1 1 2} and {1 2 3} – and a pillar taper angle of 3°. To ensure that the measured mechanical properties belong to a single grain, all pillars were inspected after deformation by SEM especially concerning continuous glide steps at the surface.

2.3.3. Bulk mechanical testing

The material supplier performed tensile tests for each HSLA steel at room temperature along the transverse direction. Rectangular specimens with a cross–section surface of 38.1 × 30 mm^2 and gauge length of 200 mm were tested.

3. Results

3.1. Characterization of constituents and bulk mechanical properties

First microstructural characterization has been done by LOM as shown in Fig. 2A–B. S1 and S2 consist of a complex mixture of polygonal ferrite and granular bainite grains (bright etched) elongated along the rolling direction with small parts of retained austenite/martensite and degenerated perlite (dark etched). EBSD measurements were conducted to assess the grain size of both samples. By fitting the grain size distribution of both samples with a log–normal function, an average grain size of (4.7 ± 0.6) µm and (4.2 ± 0.6) µm of S1 and S2 was calculated.

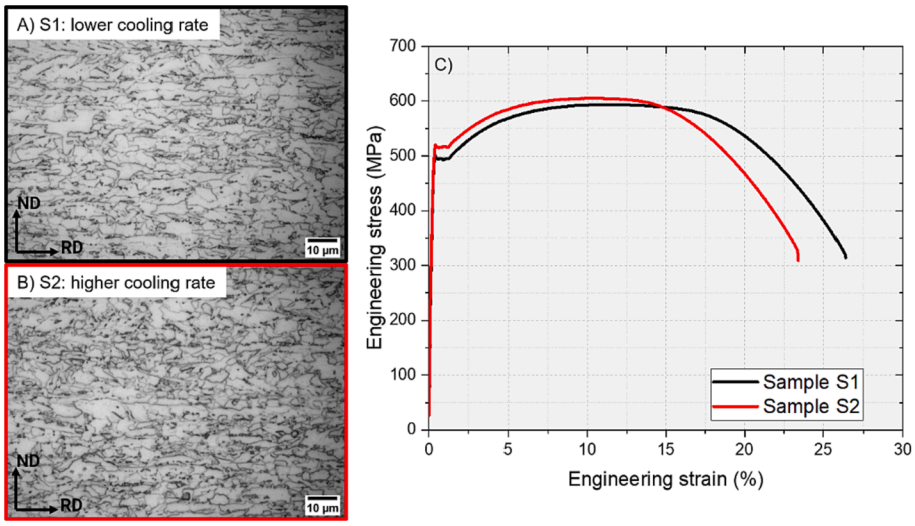

Fig. 2. The LOM images A) and B) illustrate the microstructure of S1 (lower cooling rate) and S2 (higher cooling rate), respectively. C) The engineering stress and strain curve of S1 (lower cooling rate) and S2 (higher cooling rate) was received by testing along the transverse direction of the rolled plate (RD: rolling direction).

Macroscopic tensile tests were performed to obtain the yield strength at 2% strain ($YS_{P2\%}$), ultimate tensile strength (*UTS*) and ultimate elongation of both samples (see Fig. 2C, Table 2). The higher cooling rate of S2 caused a higher *YS* and *UTS* but a smaller ultimate elongation. It is worth to note here that the $YS_{P2\%}$ from the bulk tensile test was used within this study to be consistent with the micromechanical analyses.

3.2. Dislocation density analyses of constituent phases

ECCI investigations were conducted to characterize the dislocation density of individual constituents. As described in Section 2.2, point-to-origin measurements were used to determine the phase of the selected grains, which were subsequently analyzed. For this purpose, all dislocations intersecting the image surface were counted and divided by the analyzed area ($1 \times 1\ \mu m^2$). A detailed description of the utilized technique to determine the dislocation density is given by [39]. Fig. 3A-D shows the EBSD–KAM map of a polygonal ferrite and granular bainite grain of S1 and S2, respectively. In addition, the green (polygonal ferrite example) and blue (granular bainite example) rectangles within in the KAM map denote the region of the ECCI image. A total of twelve ECCI images of different grains for each phase were analyzed to determine the average dislocation density. The orange square within the ECCI image exemplifies the analyzed $1 \times 1\ \mu m^2$ region and all the dislocation intersections are highlighted by red dots.

The ECCI images showed in general entanglements and elongated loops which are typical features of a dislocation network within a deformed material [39]. According to the applied method, a granular bainite and polygonal ferrite dislocation density of S1 and S2 was calculated; the achieved results are summarized in Fig. 4. The sample S2 with the higher cooling rate revealed a granular bainite and polygonal ferrite dislocation density of $(7.1 \pm 0.7) \times 10^{13}\ m^{-2}$ and $(2.8 \pm 0.3) \times 10^{13}\ m^{-2}$. In comparison, S1 with the lower cooling rate utilized a granular bainite and polygonal ferrite dislocation density of $(2.1 \pm 0.9) \times 10^{13}\ m^{-2}$ and $(0.9 \pm 0.1) \times 10^{13}\ m^{-2}$. This implies that the constituents of S2 contain a higher dislocation density compared to S1. Beside the dislocation density, the grain and substructure size contribute to the mechanical properties of a bulk material. Thus, further EBSD and ECCI investigations were conducted to characterize this component.

Table 2
Summary of the tensile test results and grain size of S1 and S2 measured by EBSD. The tensile tests were utilized by the material supplier along the transverse direction at room temperature. ($YS_{P2\%}$ = yield strength at 2% strain, *UTS* = ultimate tensile strength).

Sample	$YS_{P2\%}$	*UTS*	Ultimate elongation	Grain size (±error)	Cooling rate
S1	524 MPa	593 MPa	26%	4.7 ± 0.6 µm	low
S2	544 MPa	605 MPa	23%	4.2 ± 0.6 µm	high

3.3. Grain and substructure size

In general, the grain size strengthening by Hall–Petch is well known as an important factor contributing to the mechanical strength of the bulk material [40,41]. The substructure size is another intrinsic component that determines the strength of martensite and bainite [42]. Thus, systematic investigations were conducted to determine the grain size of the granular bainite and polygonal ferrite and to estimate the granular bainite substructure size. Firstly, the grain size of granular bainite and polygonal ferrite was determined by the described EBSD–KAM classification system within Section 2.2.2. Subsequently, several grains identified as granular bainite were analyzed for substructure size by conducting ECCI investigations. To achieve a first estimate about the substructure size, 60 individual measurements on each sample were conducted on several granular bainite grains. Fig. 5A shows that the polygonal ferrite grain size is equivalent for S1 (2.3 ± 0.03) µm and S2 (2.4 ± 0.03) µm, while the grain size of granular bainite is smaller in case of S1 (9.5 ± 0.56) µm compared to S2 (11.2 ± 0.95) µm. In addition, it can be seen that the ECCI investigations revealed a substructure size of (2.9 ± 0.15) µm and (1.9 ± 0.10) µm in case of S1 and S2, respectively. Fig. 5B–C further illustrates this with two representative images of two granular bainite grains taken from S1 and S2. The grain area of both grains is highlighted by a dashed orange (S1) and blue (S2) line. The changing contrast between the sub–blocks indicates that the higher cooling rate led to a smaller substructure size compared to S1. The result from the ECCI investigations are comparable to the reported results elsewhere [8,43,44]. Consequently, the application of a higher cooling rate led to a constant polygonal ferrite size. The granular bainite grains were coarser whereas the substructure size decreased by utilizing a higher cooling rate and agrees with the literature.

3.4. Pillar compression tests

Micropillar compression tests were performed to determine the CRSS of granular bainite and polygonal ferrite which both consist of a bcc

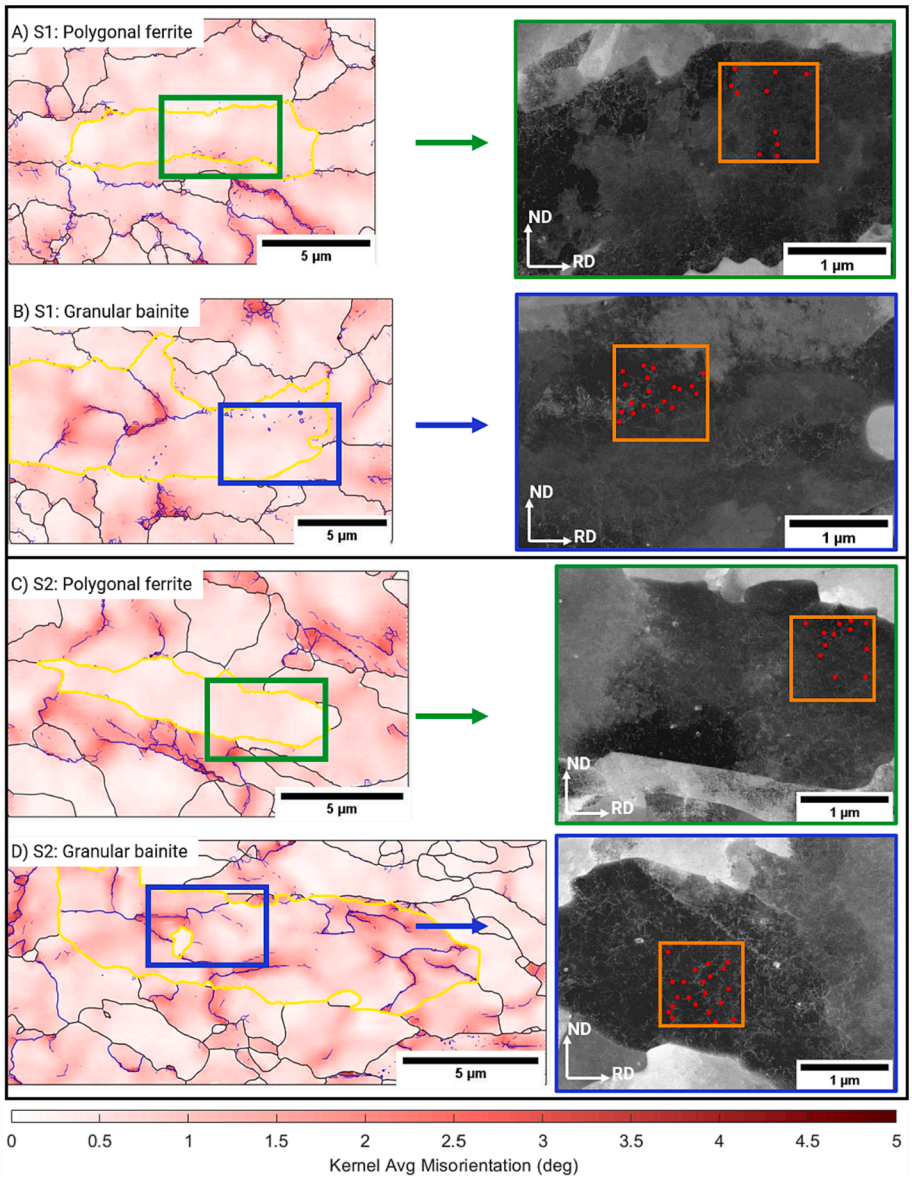

Fig. 3. A), B) and C), D) shows the EBSD–KAM map and the ECCI image of a polygonal ferrite and granular bainite grain from S1 (lower cooling rate) and S2 (higher cooling rate), respectively. The orange square within the ECCI image exemplifies the analyzed $1 \times 1\ \mu m^2$ region and all the dislocation intersections are highlighted by a red dot. (For interpretation of the references to color in this figure legend, the reader is referred to the web version of this article.)

crystal structure. Subsequently, the engineering stress and engineering strain was calculated using the center diameter and the height of the pillar. Fig. 6A–D illustrates a representative engineering stress and strain curve for each constituent of samples S1 and S2. The polygonal ferrite curves are displayed by bold line whereas the granular bainite is displayed by a dashed line. The color is referred to the activated slip system and shows in all cases a typical intermittent flow which has been commonly observed in the used pillar size regime [18,36]. The pillar compression tests revealed that all three slip systems were activated within the polygonal ferrite grains. Only two of them were activated by performing pillar compression tests in the granular bainite constituent. It is also evident from Fig. 6A–D that the granular bainite revealed a higher engineering stress level in both samples compared to the tested polygonal ferrite grains. The CRSS was calculated based on the engineering stress at 2% strain $\sigma_{2\%}$ and the Schmid factor m of the activated slip system.

Fig. 7-F shows representative pillars of S1 and S2 and the predicted slip systems according to the crystallographic orientation. All six examples illustrate that one slip system was preferentially activated until an engineering strain of 5 – 15% was reached. Subsequently, the activated slip system was identified by superimposing the predicted slip planes having the four highest Schmid factors with the *post mortem* pillar image. The corresponding values regarding the shown activated slip plane, the related Schmid factor and the calculated CRSS are shown on each SEM image. It is worth to note that not necessarily the first activated slip system had the highest Schmid factor. Moreover, the activated slip system was identified once the predicted glide plane coincided with the post mortem pillar image. Two examples are added in the supplementary information to illustrate that some uncertainty is present for identifying the activated slip system. In these cases, the differences in angles between the glide planes is less than 7°, which leads to an uncertainty regarding the slip plane identification. It is assumed that this influenced the CRSS with an error of approx. ± 4%.

The average CRSS for S1 and S2 was fitted by a Gaussian distribution and plotted as a cumulative probability function seen in Fig. 8A-B. In addition, the 90% and 95% confidence band intervals are displayed for each constituent. Polygonal ferrite and granular bainite of S1 reached a CRSS of (153 ± 4) MPa and (194 ± 6) MPa, respectively (see Fig. 8A).

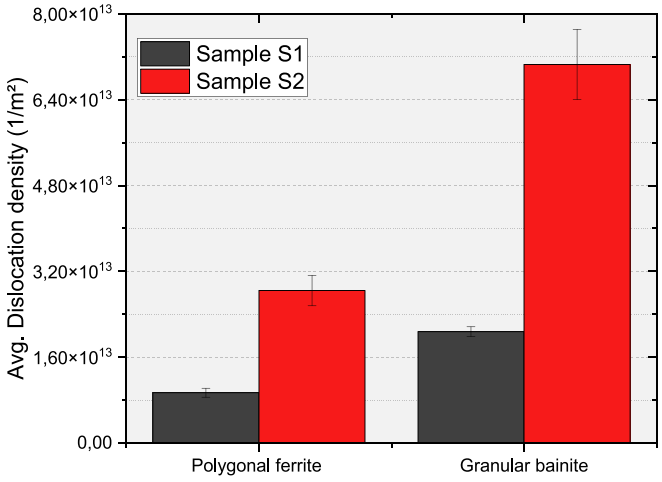

Fig. 4. The average dislocation density is shown for S1 and S2 and each constituent. The average value and its corresponding average error was obtained by measuring 12 independent positions with an area of 1 × 1 μm^2.

Due to the higher dislocation content of S2, polygonal ferrite and granular bainite had an average CRSS of (183 ± 7) MPa and (221 ± 7) MPa. Consequently, the CRSS of both constituents increased by 16% (polygonal ferrite) and 12% (granular bainite) by applying a higher cooling rate. Moreover, the cumulative probability function of S1 shows a clear separation between both constituents whereas the CRSS of polygonal ferrite and granular bainite of S2 appeared as a smooth transition as displayed in Fig. 8B. The performed experiments revealed that the average CRSS of both constituents increased by using a higher cooling rate. It is noticeable that the difference in average CRSS between polygonal ferrite and granular bainite of the same sample and even the difference in average CRSS of polygonal ferrite and granular bainite between S1 and S2 was almost identical.

Once the CRSS of each constituent and sample was determined, the results were analyzed regarding the activated slip plane family as shown in Fig. 8C–F. The pillar compression tests revealed that all three slip systems – {1 1 0}, {1 1 2} and {1 2 3} – were activated regarding polygonal ferrite at S1 and S2. On the other hand, pillar compression tests within granular bainite grains did not activate the {1 1 2} and {1 1 0} slip system on sample S1 and S2, respectively. One can further conclude that the cumulative probability function and the average CRSS of the distinct slip plane families are comparable.

In addition, Fig. 9 compares the activated slip systems of S1 and S2 with the color–coded regions for each slip system according to Schmid's law assuming an identical CRSS for all slip systems. The inverse pole figure (IPF) illustrates that the majority of the tested pillar follows Schmid's law and the crystallographic orientation of the main outliers are next to the border between two different colored regions. The breakdown of Schmid's law and the stress concentration at the pillar top surface are mainly considered to be responsible for activating slip systems with a lower Schmid factor [45,46]. This will be discussed in the section below.

4. Discussion

The first part of the discussion (Section 4.1) addresses the determination of bulk behavior through pillar compression tests within polygonal ferrite and granular bainite grains. Afterwards, Section 4.2 deals with the strengthening mechanism which were considered to be responsible for the higher strength level of the bulk material and the individual constituents of S1 and S2. Finally, Section 4.3 is dedicated to the activated slip systems by performing pillar compression tests.

4.1. Micromechanical tests compared to the bulk behavior

Tensile tests on the investigated materials indicated that the higher cooling rate of S2 resulted in a higher $YS_{P2\%}$ and *UTS* compared to S1 (see Fig. 2D and Table 2). The performed microcompression tests revealed that the polygonal ferrite and granular bainite *CRSS* were affected by the different cooling rate (see Fig. 8A-B). In order to compare the micromechanical behavior with the tensile tests of the bulk material, the phase fractions of granular bainite C_{GB} and polygonal ferrite C_{PF} was determined for S1 and S2 by utilizing the EBSD-KAM classification as described in Section 2.2.2. Subsequently, the rule of mixture was used to calculate the *CRSS* of the bulk material ($CRSS_{bulk}$) by using Equation 1A and 1B:

$$CRSS_{bulk} = CRSS_{PF}{}^{*}C_{PF} + CRSS_{GB}{}^{*}C_{GB} \quad and \tag{1A}$$

$$C_{PF} + C_{GB} = 1 \tag{1B}$$

where, $CRSS_{PF}$ and $CRSS_{GB}$ represents the *CRSS* of granular bainite and polygonal ferrite based on the pillar compression tests. The Taylor factor *M* correlates the *YS* of the polycrystalline bulk material with the $CRSS_{Bulk}$ which is calculated by Eq. (2) [47,48]. Hence, the yield strength $YS_{calc.}$ of the bulk material was calculated by using Eq. (2):

$$YS_{calc.} = M^{*}CRSS_{bulk}. \tag{2}$$

A previous computer simulation considered all three possible bcc slip systems along the ⟨111⟩ direction and revealed an average Taylor factor of $M_{Avg.} = 2.733$ for compression and tension for grains of various orientations [49]. This value was chosen, since the pole figure of the

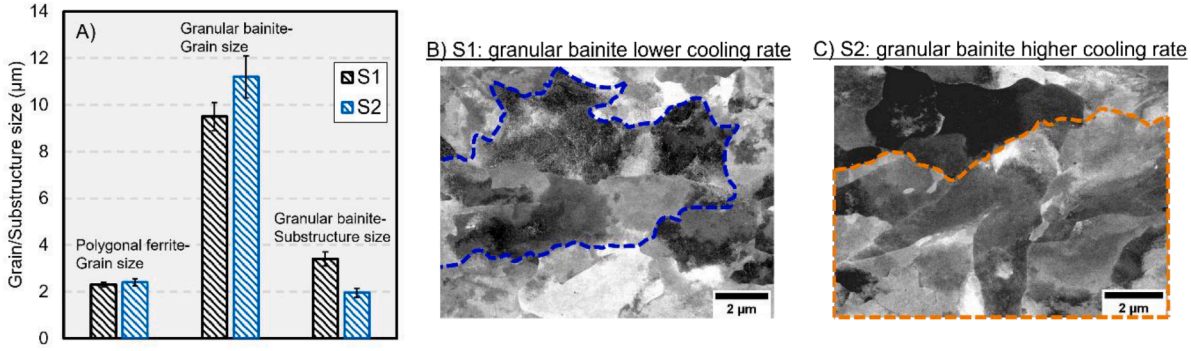

Fig. 5. A) The granular bainite and polygonal ferrite grain size was calculated based on EBSD files. ECCI investigations were conducted to reveal the granular bainite substructure size by 60 manual measurements. The error bars indicating the corresponding average error. B) and C) Two representative examples of the granular bainite substructure. The area which belongs to the selected grain is indicated by a blue (S1) and orange (S2) dashed line. The grains were defined by a grain tolerance angle of 5°. (For interpretation of the references to color in this figure legend, the reader is referred to the web version of this article.)

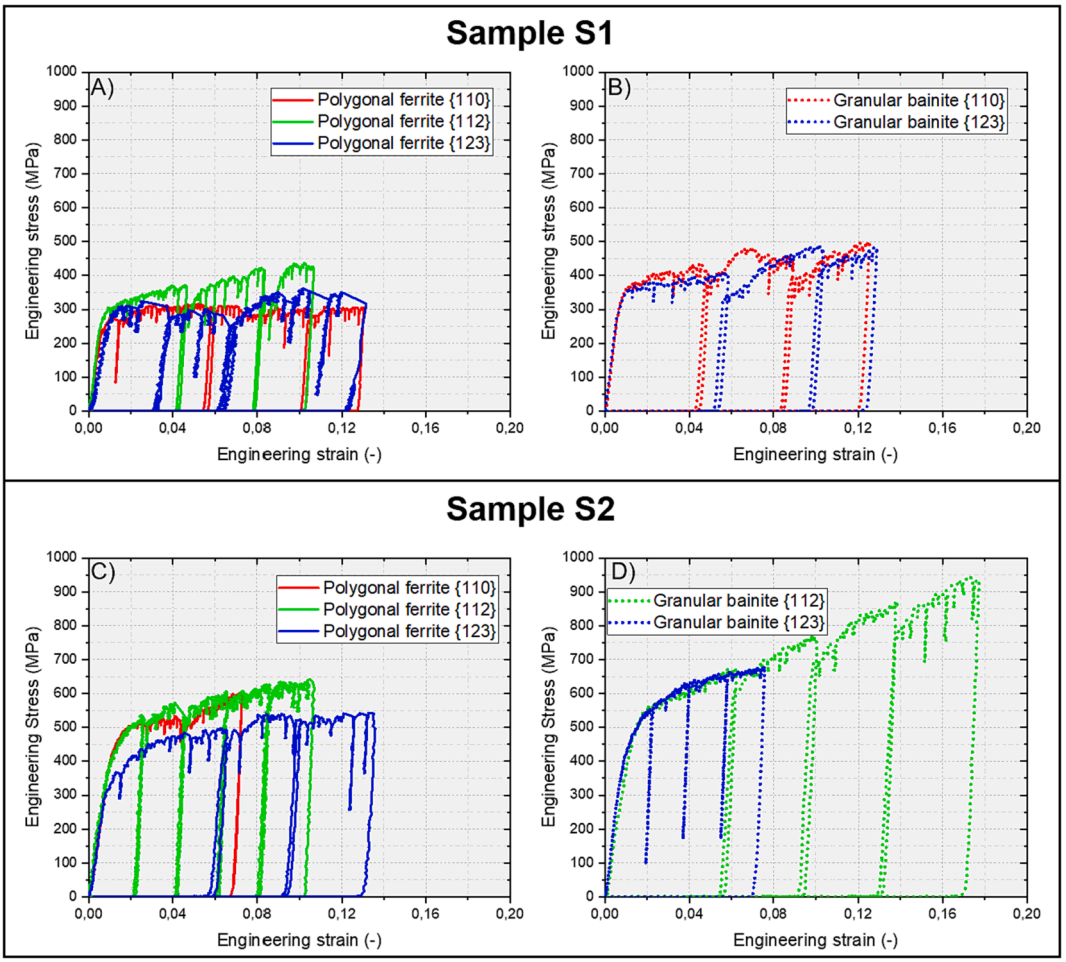

Fig. 6. A) and B) shows a representative example for polygonal ferrite and granular bainite of S1. C) and D) indicates the representative example for polygonal ferrite and granular bainite of S2. The engineering stress and engineering strain curves obtained from polygonal ferrite grains are shown by bold lines whereas the granular bainite results are shown by dashed lines. The color indicates the activated slip system: {1 1 0} = red, {1 1 2} = green, {1 2 3} = blue. (For interpretation of the references to color in this figure legend, the reader is referred to the web version of this article.)

investigated samples showed a random polycrystalline orientation distribution. Consequently, a macroscopic yield strength $YS_{calc.}$ of 480 MPa and 572 MPa was calculated for S1 and S2, respectively. To summarize this, all experimental and calculated results are listed in Table 3.

It is shown that $YS_{calc.}$ and $YS_{2\%}$ coincide and deviate by only 8% and 5% for S1 and S2, respectively. The deviation between $YS_{calc.}$ and $YS_{2\%}$ may be caused by the fact that single grains were tested by pillar compression tests allowing for free and unconstrained slip. This can explain the underestimation of $YS_{2\%}$ by the CRSS, but not the overestimation. A prior work has studied different ratios between wire diameter to grain size by tensile experiments [50]. This study ascertained that the yield stress of a micro–sized wire varies if the ratio is below 10. In addition to the single polygonal ferrite grains, granular bainite grains with a substructure were also tested (see Fig. 5B and C). Since the performed ECCI investigations on S1 and S2 determined a granular bainite substructure size of (2.9 ± 0.15) μm and (1.9 ± 0.10) μm and a pillar diameter of 2 μm was used, it is evident that a maximum of one to three sub–grains can be contained in the pillar volume. Subsequently, the variation of the number of sub–grains in the pillar volume may contribute to the deviation between $YS_{calc.}$ and $YS_{2\%}$.

Since the pillar position can vary slightly inside the individual grains, an inhomogeneous distribution of dislocations inside the constituents will also result in a variation of dislocations inside the tested pillar volume. Thus, the small overestimation of $YS_{calc.}$ compared to $YS_{2\%}$ can also be related to a dislocation density that is slightly higher in the pillar volume compared to the average dislocation density based on the ECCI investigations.

The arrangement and shape of the individual phases relative to each other also contributes to the overall bulk behavior. It has been shown on ferritic–martensitic steels that the morphology of the constituents had a significant impact on the mechanical behavior [51,52]. Both investigations observed a higher strength and lower ductility at samples with large and equiaxed martensite particles compared to microstructures with elongated martensite islands; these results were achieved from samples with a constant composition and phase fraction. Subsequently, the relative distribution of polygonal ferrite and granular bainite grains to each other may contribute to the differences between $YS_{calc.}$ and $YS_{2\%}$. This aspect has not been considered within the EBSD–KAM classification system [32].

4.2. Strengthening mechanisms

It can be assumed that the mechanical strength of a complex microstructure can be decomposed into a number of intrinsic components [4,42]. In general, the following mechanisms are responsible for determining the mechanical strength: yield strength of pure iron, solid solution hardening, precipitation hardening, dislocation hardening, grain and sub–grain size (Hall–Petch) and a possible texture contribution [4]. The scope of this work was on characterizing the micromechanical behavior and microstructure and substructure size. Subsequently, the effect of grain and sub–grain size (“smaller is stronger”) and dislocation density on the macroscopic strength are discussed.

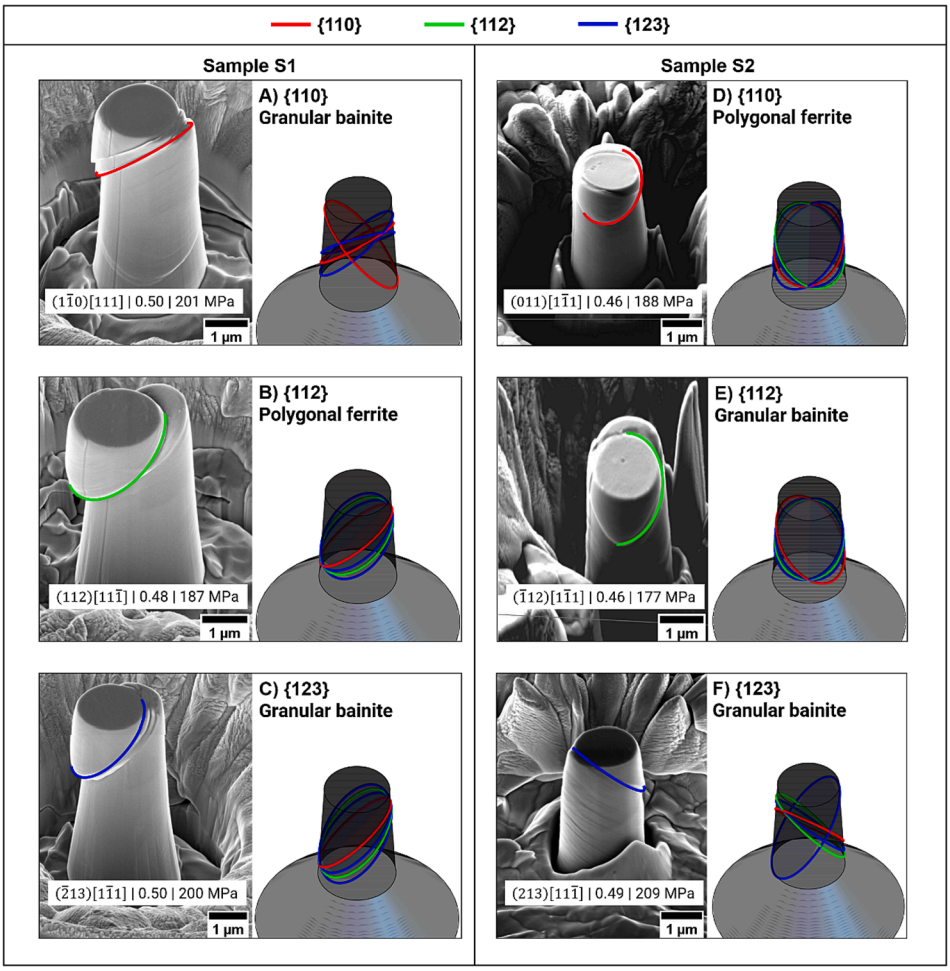

Fig. 7. Slip trace analysis shown on three representative *post mortem* pillar images for S1 (column 1 A–C) and S2 (column 2 D–F). The activated slip traces of {1 1 0}, {1 1 2} and {1 2 3} of the *post mortem* images were superimposed with the predicted slip traces as shown in A), B) and C) for S1 and D), E) and F) for S2, respectively. In addition, the activated slip plane, the corresponding Schmid factor and the CRSS (based on the compressive yield strength at 2% strain) are indicated specified on each SEM image.

The tensile tests of the bulk material determined a higher $YS_{P2\%}$ and *UTS* at material S2 by using a higher cooling rate compared to material S1 (see Fig. 2C). In general, granular bainite forms by the onset of a displacive transformation and the substructure size depends on the applied cooling rate [8,14]. Previous TEM investigations demonstrated that the granular bainite substructure changes from a lath/sheaf substructure to equiaxed–large grains by varying the cooling rate from 60 to 5 K/s [24]. This agrees to the achieved results, since the performed ECCI investigations ascertained a granular bainite substructure size of (2.9 ± 0.15) µm and (1.9 ± 0.10) µm on the investigated material S1 and S2, respectively. Subsequently, the application of a higher cooling rate produced a smaller substructure separated by sub–boundaries.

The phase fraction was determined as described in Section 2.2.2 and revealed that S1 is composed of 74% granular bainite and S2 contained 56% despite the higher cooling rate of S2 (see Table 3). This agrees with the misorientation angle distribution based on the EBSD measurements (see Fig. 10). The higher fraction of misorientation angles between 35 and 63° may indicate that more polygonal ferrite grains were formed despite the higher cooling rate of S2. It was recently shown that the application of a lower cooling rate leads to the formation of a coarser substructure [24,53]. Thus, the lower cooling rate causes within the high–temperature range a flattened dislocation cell structure by pile–up or tangled dislocations and the polygonization process has more time to proceed and a coarser substructure may emerge [24]. In addition, the smaller cooling rate and subsequently higher transformation temperature reduces the density of sub-boundaries [53,54]. Indeed, the coarser granular bainite grains of S1 still include a high fraction of strain gradients which are between 3 and 5°. This results in a higher granular bainite fraction per area compared to a microstructure which was treated by a faster continuous cooling process.

The performed pillar compression tests revealed that the application of a higher cooling rate (in case of sample S2) led to a higher CRSS for granular bainite and polygonal ferrite (see Fig. 8A and B). A previous study performed pillar compression tests on a dual–phase steel containing polygonal ferrite and martensite [18]. The same pillar size was used as in the present study and the results of both investigations coincide regarding the CRSS of polygonal ferrite. However, to the authors best knowledge, no results have been published on pillar compression associated with granular bainite.

The ECCI investigations revealed that both constituents of S2 contained a higher dislocation density compared to S1 and resulted in a higher CRSS (see Fig. 4). It is also interesting to note that the polygonal ferrite of S2 had a higher dislocation density as well as a higher CRSS than the granular bainite phase of S1. A previous study revealed a granular bainite and polygonal ferrite dislocation density of $1.7 \times 10^{14}\ m^{-2}$ and $0.37 \times 10^{14}\ m^{-2}$ by TEM investigations, respectively [55]. More recently, Huang et al. [8] also measured a granular bainite dislocation density of $(5.4 \pm 0.9) \times 10^{14}\ m^{-2}$. Consequently, both aforementioned studies exhibited a slightly higher dislocation density for the investigated constituents. This could be caused by utilizing a lower

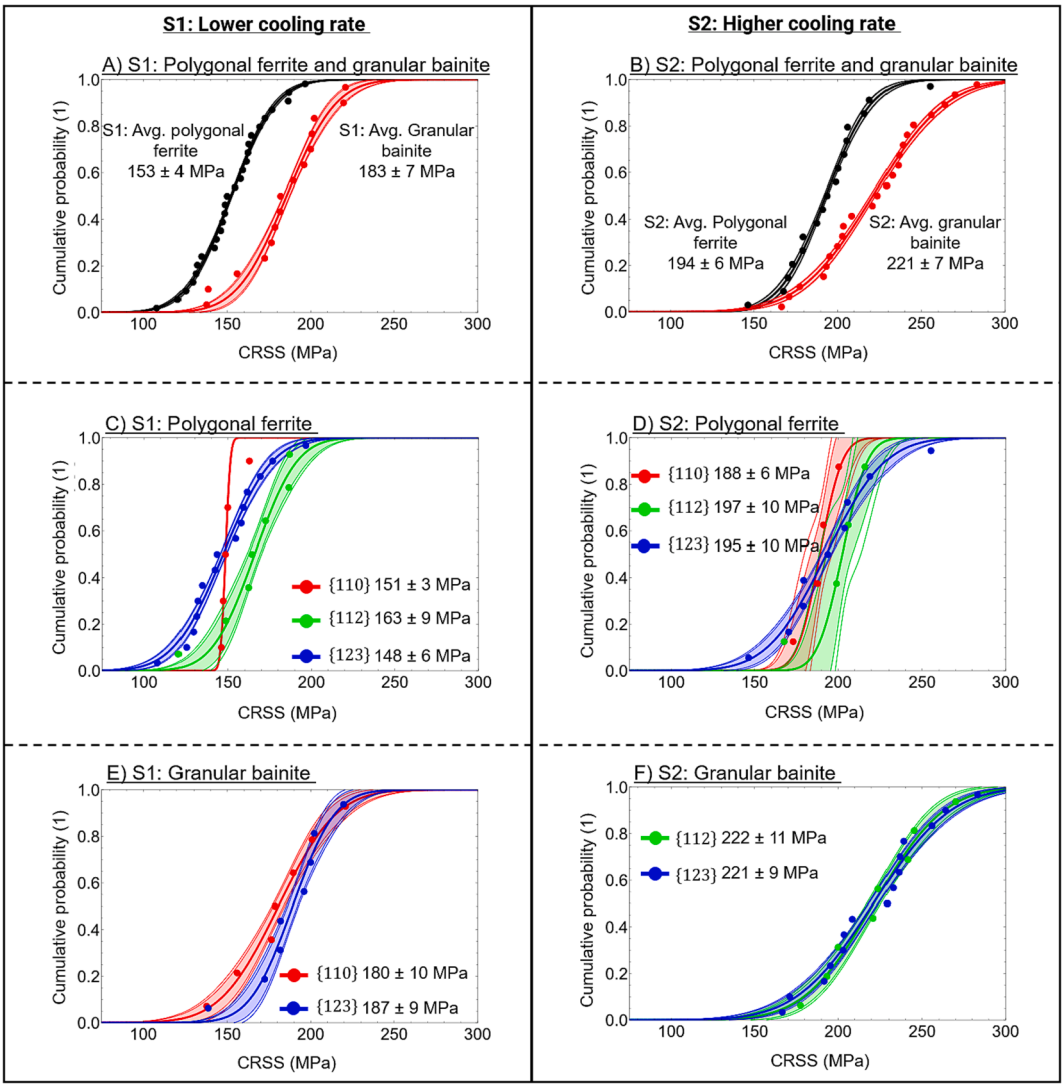

Fig. 8. The average CRSS of S1 A) and S2 B) was calculated for each constituent (polygonal ferrite and granular bainite) based on the engineering stress $\sigma_{2\%}$ and plotted with the cumulative probability function. C) and D) shows the CRSS of the activated slip planes for polygonal ferrite and granular bainite of S1. E) and F) also illustrates the CRSS of polygonal ferrite and granular bainite but for S2. A Gaussian function was used to achieve the average CRSS and its error. In addition, the 90% and 95% confidence band intervals are plotted for cumulative probability curves.

cooling rate. Here it is worth to note, that the measured dislocation density served as a representative measurement for each constituent and does not necessarily represent the accurate dislocation density.

The increased strength of S2 can be correlated to the presence of a higher dislocation density inside the activated pillar volume. Subsequently, more dislocations can move on the activated slip system with the highest Schmid factor [56]. Dislocation glide can be impeded by the interaction with other mobile or immobile dislocations and results in a higher CRSS [4]. Moreover, granular bainite grains of S2 contained a smaller substructure size than S1 (see Fig. 5A). It is obvious that this contributes to the bulk strengthening as well. A former investigation determined for a low carbon steel with a fully bainitic structure that the yield stress is proportional to the inverse lath size defined with low boundary misorientation (2 – 7°) [27]. It was concluded that lath boundaries and dislocation cell boundaries acting as obstacles to the moving dislocations. This is also consistent with other studies on the strength increase due to the refinement of the granular bainite substructure size [9,10,28].

One can also recognize that the polygonal ferrite of S1 showing a lower CRSS compared to the polygonal ferrite grains of S2. Moreover, the bulk tensile test ascertained that material S1 has a lower *YS* compared to S2 (see Fig. 2C). In a recent study [18], pillar compression tests were performed on two different ferrite–martensite steels. It was found out that the softer ferrite phase determined the onset of yielding of the bulk material [18]. This is in agreement with the current results, since S2 contained a higher $YS_{2\%}$ and polygonal ferrite dislocation density. It is assumed that the higher cooling rate of S2 introduced more dislocations inside the polygonal ferrite during the displacive transformation of the granular bainite phase [24]. Subsequently, the higher dislocation density served as obstacles and increased the CRSS to move the activated dislocations [17,28,56].

The precipitation strengthening by the formation of carbo–nitrides has been identified as a further mechanism contributing to the mechanical strength [26,28]. Since the tested material contained Nb and Ti additions, it is possible that carbo–nitrides were formed during the production process. Previous TEM investigations showed that their size varies within the nanometer range [26,28]. Thus, carbo–nitrides precipitates can be also included within the tested pillar volume. In general, precipitates nucleate and grow during the cooling process and cross different slip planes [56]. Once mobile dislocations are moving along the activated slip plane and precipitates acting as obstacles from sliding further, they must either cut through or bow out between the particles

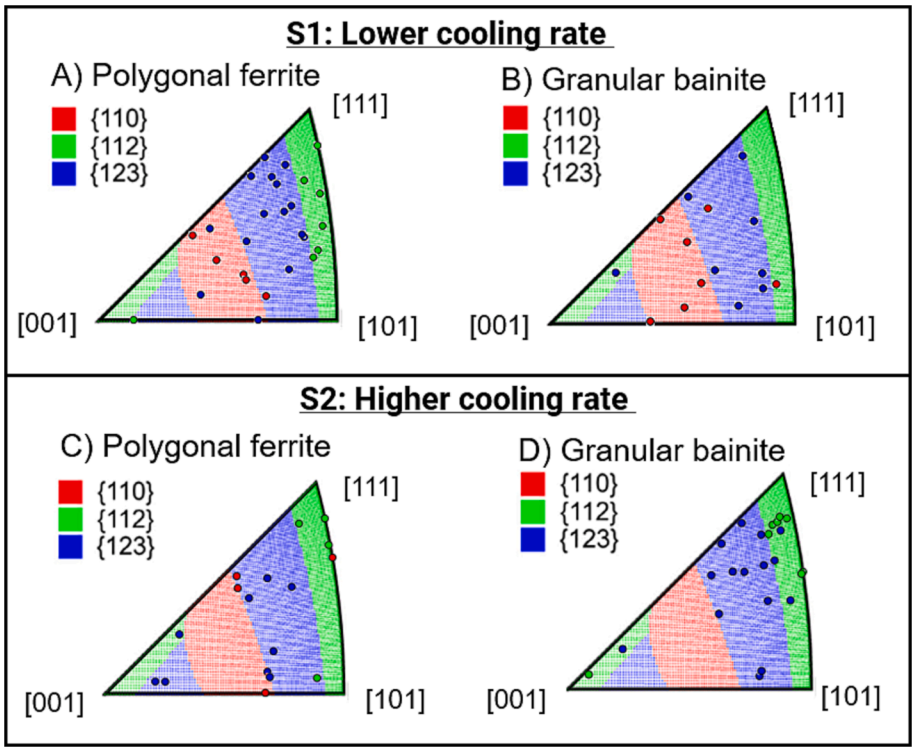

Fig. 9. A) and B) represents the activated slip system during the pillar compression tests within polygonal ferrite and granular bainite grains. C) and D) also indicates the orientation of the activated slip system for S1 and its constituent's polygonal ferrite and granular bainite. The color–coded areas within each IPF exhibits the region where the {1 1 0}, {1 1 2} and {1 2 3} slip system has the highest Schmid factor by assuming the same CRSS for all slip systems.

Table 3
All experimental and calculated results are summarized to compare the mechanical behavior of the bulk material and the individual tested phases. The estimated bulk yield strength is given with its standard deviation (PF = Polygonal ferrite / GB = Granular bainite).

Source	CRSS Pillar compression		Tensile test bulk material	Literature [49]	EBSD	Calculated bulk yield strength
Sample	Polygonal ferrite	Granular bainite	$YS_{P2\%}$	Taylor factor	Phase fraction	$YS_{calc.}$
S2	(153 ± 4) MPa	(183 ± 7) MPa	524 MPa	2.733	26% / 74% PF / GB	480 MPa ± 2%
S2	(194 ± 6) MPa	(221 ± 7) MPa	544 MPa		44% / 56% PF / GB	572 MPa ± 2%

[56,57]. Additional TEM investigations were not conducted to quantify the precipitates and, thus interfere with the dislocation strengthening mechanism within the tested pillar volume.

4.3. Activated slip systems

The performed pillar compression tests utilized that all three bcc slip systems - namely {1 1 0}, {1 1 2} and {1 2 3} - were activated within polygonal ferrite grains (see Fig. 8C and D). This agrees well to the observation from a previous study [18] on pillar compression tests of polygonal ferrite grains in two different DP steels. In contrast, testing granular bainite grains did not show the activation of all three slip systems for each sample. The slip systems {1 1 2} and {1 2 3} were activated by testing granular bainite grains on S1 whereas only the {1 1 2} and {1 2 3} slip systems were observed for granular bainite grains on S2 (see Fig. 8E and F). It should be noted that all slip planes were identified using SEM images and are therefore limited by the resolution of a field emission microscope. It was concluded by previous TEM experiments and atomistic simulations that the occurrence of {1 1 2} and {1 2 3} slip system is caused by the cross slip of screw dislocations on {1 1 0} planes [45,58,59]. It has been shown that this also results in a wavy slip pattern due to the cross slip of screw dislocations [58–60]. Since the a wavy-slip is not visible on the microscale and the predicted slip traces based on Schmid's law coincide with the *post mortem* images, it was assumed that Schmid's law can be applied. The cross slip of screw dislocations on {1 1 0} planes could also explain why the CRSS for all activated slip systems of granular bainite and polygonal ferrite for each sample was nearly identical. The fact that only two out of three slip systems were activated at the granular bainite could merely be a statistical problem as only 15 and 23 pillars were tested for S1 and S2, respectively.

In addition, it can be concluded that nearly all tested pillars followed Schmid's law according to the IPF indicating the regions with the highest Schmid factor and the experimentally identified slip systems (see Fig. 9). The second slip system was activated only for a few outliers when the Schmid factor of the first two was nearly identical. This is related to the limited number of dislocation sources within the confined pillar volume [46,61]. Furthermore, the smallest pillar diameter at the top caused lateral stresses during loading and could further be responsible that not the primary slip system was activated [36].

5. Summary

In the present work, two samples (S1 and S2) were tested with the same chemical composition but a different cooling rate was applied during the production process. This led to microstructural changes in the

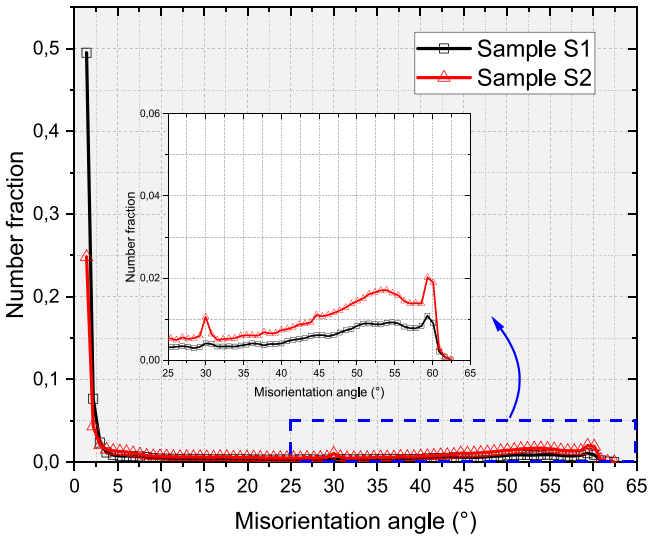

Fig. 10. The average misorientation angle distribution of S1 (black data) and S2 (red data) is shown based on EBSD measurements. It is indicated that S2 contains a higher fraction of grain boundaries with a misorientation angle between 35 and 63°. (For interpretation of the references to color in this figure legend, the reader is referred to the web version of this article.)

polygonal ferrite and granular bainite phases. Tensile tests of the bulk material revealed a high yield and tensile strength by using a higher cooling rate in case of S2. However, both constituents have not been characterized regarding their micromechanical properties. Thus, the aim of this study was to perform micropillar compression tests to characterize the micromechanical strength of the individual constituents, since it was not clarified which mechanism caused the different mechanical strength of the bulk material. Beside pillar compression tests to quantify the CRSS of the activated slip system, ECCI and EBSD investigations were conducted to elucidate the strengthening mechanism by measuring the grain-, sub–grain size and the dislocation density. The key findings of the present study are summarized by the following points:

- Pillar compression tests revealed that the CRSS of polygonal ferrite and granular bainite increased approx. 30 MPa by using a higher cooling rate for S2. It was shown that even the polygonal ferrite of S2 has a higher CRSS with (194 ± 6) MPa than the granular bainite of S1 with (183 ± 7) MPa. This agrees well with the measured dislocation density by ECCI investigations. Since the tested pillar volume contained only one to three sub-grains of the granular bainite substructure, it is reasonable that the three- and fourfold higher dislocation density within the polygonal ferrite and granular bainite from sample S2 mainly contributed to the increasing CRSS. Nearly all compression tests followed Schmid's law. All three possible slip systems were confirmed by *post mortem* images in case of polygonal ferrite grains. Micropillars placed within granular bainite grains showed only the activation of two slip systems.
- Consequently, both phases were strengthened by increasing the cooling rate. It is assumed that the smaller granular bainite substructure size (S1 (9.5 ± 0.56) μm compared to S2 (11.2 ± 0.95) μm) contributed beside the higher dislocation density to the increasing strength of S2.
- Based on ECCI investigations, an increasing dislocation density was measured for polygonal ferrite (S1: (0.9 ± 0.1) × 10^{13} m^{-2} and S2: (2.8 ± 0.3) × 10^{13} m^{-2}) and granular bainite (S1: (2.1 ± 0.9) × 10^{13} m^{-2} and S2: (7.1 ± 0.7) × 10^{13} m^{-2}) grains as well. It was concluded that this was caused by the higher cooling rate.

Declaration of Competing Interest

The authors declare that they have no known competing financial interests or personal relationships that could have appeared to influence the work reported in this paper.

Data availability

Data will be made available on request.

Acknowledgement

The authors gratefully acknowledge the funding of this project and for supplying the sample material by the steel manufacturer AG der Dillinger Hüttenwerke. C.K. and G.D. are also grateful for the financial support of the German Research Foundation (Deutsche Forschungsgemeinschaft, DFG) within the Collaborative Research Center (TRR 188, "Damage Controlled Forming Processes", 278868966) in project B03 "Understanding the damage initiation at microstructural scale".

References

[1] S. Zajac, V. Schwinn, K.H. Tacke, Characterisation and Quantification of Complex Bainitic Microstructures in High and Ultra-High Strength Linepipe Steels, Mater. Sci. Forum 500–501 (2005) 387–394, https://doi.org/10.4028/www.scientific.net/msf.500-501.387.
[2] Z.J. Xie, X.P. Ma, C.J. Shang, X.M. Wang, S.V. Subramanian, Nano-sized precipitation and properties of a low carbon niobium micro-alloyed bainitic steel, Mater. Sci. Eng. A 641 (2015) 37–44, https://doi.org/10.1016/j.msea.2015.05.101.
[3] W.B. Lee, S.G. Hong, C.G. Park, S.H. Park, Carbide precipitation and high-temperature strength of hot-rolled high-strength, low-alloy steels containing Nb and Mo, Metall Mater Trans A Phys Metall Mater Sci. 33 (2002) 1689–1698, https://doi.org/10.1007/s11661-002-0178-2.
[4] T.N. Baker, Microalloyed steels, Ironmak. Steelmak. 43 (2016) 264–307, https://doi.org/10.1179/1743281215Y.0000000063.
[5] G. Krauss, S.W. Thompson, Ferritic Microstructures in Continuously Cooled Low- and Ultralow-carbon Steels, ISIJ Int. 35 (1995) 937–945, https://doi.org/10.2355/isijinternational.35.937.
[6] S.W. Thompson, D.J. Vin Col, G. Krauss, Continuous cooling transformations and microstructures in a low-carbon, high-strength low-alloy plate steel, Metall. Trans. A 21 (1990) 1493–1507, https://doi.org/10.1007/BF02672564.
[7] B.X. Wang, X.H. Liu, G.D. Wang, Correlation of microstructures and low temperature toughness in low carbon Mn–Mo–Nb pipeline steel, Mater. Sci. Technol. 29 (2013) 1522–1528, https://doi.org/10.1179/1743284713Y.0000000326.
[8] B.M. Huang, J.R. Yang, H.W. Yen, C.H. Hsu, C.Y. Huang, H. Mohrbacher, Secondary hardened bainite, Mater. Sci. Technol. (United Kingdom). 30 (2014) 1014–1023, https://doi.org/10.1179/1743284714Y.0000000536.
[9] H. Sheng Fang, C. Feng, Y. Kang Zheng, Z. Gang Yang, B. Zhe Bai, Creation of Air-Cooled Mn Series Bainitic Steels, J. Iron Steel Res. Int. 15 (2008) 1–9, https://doi.org/10.1016/S1006-706X(08)60257-5.
[10] X.N. Xu, Y. Tian, Q.B. Ye, R.D.K. Misra, Z.D. Wang, The Significant Impact of the Characteristics of Granular Structure and Granular Bainite on the Mechanisms Contributing to Strength-Ductility Combination, J Mater Eng Perform. 30 (2021) 7479–7487, https://doi.org/10.1007/s11665-021-05887-x.
[11] M. Müller, D. Britz, L. Ulrich, T. Staudt, F. Mücklich, Classification of bainitic structures using textural parameters and machine learning techniques, Metals (Basel). 10 (2020) 1–19, https://doi.org/10.3390/met10050630.
[12] L.J. Habraken, M. Economopoulos, Bainitic microstructures in low-carbon alloy steels and their mechanical properties, (1967).
[13] B.L. Bramfitt, J.G. Speer, A perspective on the morphology of bainite, Metall. Trans. A 21 (1990) 817–829, https://doi.org/10.1007/BF02656565.
[14] H.K.D.H. Bhadeshia, Bainite in steels: theory and practice, CRC Press, 2019.
[15] H. Ghassemi-Armaki, P. Chen, S. Bhat, S. Sadagopan, S. Kumar, A. Bower, Microscale-calibrated modeling of the deformation response of low-carbon martensite, Acta Mater. 61 (2013) 3640–3652, https://doi.org/10.1016/j.actamat.2013.02.051.
[16] F. Roters, M. Diehl, P. Shanthraj, P. Eisenlohr, C. Reuber, S.L. Wong, T. Maiti, A. Ebrahimi, T. Hochrainer, H.O. Fabritius, S. Nikolov, M. Friák, N. Fujita, N. Grilli, K.G.F. Janssens, N. Jia, P.J.J. Kok, D. Ma, F. Meier, E. Werner, M. Stricker, D. Weygand, D. Raabe, DAMASK – The Düsseldorf Advanced Material Simulation Kit for modeling multi-physics crystal plasticity, thermal, and damage phenomena from the single crystal up to the component scale, Comput Mater Sci. 158 (2019) 420–478, https://doi.org/10.1016/j.commatsci.2018.04.030.
[17] H. Ghassemi-Armaki, R. Maaß, S.P. Bhat, S. Sriram, J.R. Greer, K.S. Kumar, Deformation response of ferrite and martensite in a dual-phase steel, Acta Mater. 62 (2014) 197–211, https://doi.org/10.1016/j.actamat.2013.10.001.

[18] C. Tian, D. Ponge, L. Christiansen, C. Kirchlechner, On the mechanical heterogeneity in dual phase steel grades: Activation of slip systems and deformation of martensite in DP800, Acta Mater. 183 (2020) 274–284, https://doi.org/10.1016/j.actamat.2019.11.002.
[19] J.L. Stewart, L. Jiang, J.J. Williams, N. Chawla, Prediction of bulk tensile behavior of dual phase stainless steels using constituent behavior from micropillar compression experiments, Mater. Sci. Eng. A 534 (2012) 220–227, https://doi.org/10.1016/j.msea.2011.11.062.
[20] M. Pozuelo, J.W. Stremfel, J.M. Yang, J. Marian, Strengthening to softening transition in lath martensite, Materialia (Oxf). 5 (2019), 100254, https://doi.org/10.1016/j.mtla.2019.100254.
[21] S. Morito, H. Tanaka, R. Konishi, T. Furuhara, T. Maki, The morphology and crystallography of lath martensite in Fe-C alloys, Acta Mater. 51 (2003) 1789–1799, https://doi.org/10.1016/S1359-6454(02)00577-3.
[22] P. Chen, H. Ghassemi-Armaki, S. Kumar, A. Bower, S. Bhat, S. Sadagopan, Microscale-calibrated modeling of the deformation response of dual-phase steels, Acta Mater. 65 (2014) 133–149, https://doi.org/10.1016/j.actamat.2013.11.036.
[23] W.B. Morrison, Overview of microalloying in steel, Report 25–35 (2000).
[24] S. Jun Jia, B. Li, Q. You Liu, Y. Ren, S. Zhang, H. Gao, Effects of continuous cooling rate on morphology of granular bainite in pipeline steels, J. Iron Steel Res. Int. 27 (2020) 681–690, https://doi.org/10.1007/s42243-019-00346-3.
[25] Y.W. Chen, B.M. Huang, Y.T. Tsai, S.P. Tsai, C.Y. Chen, J.R. Yang, Microstructural evolutions of low carbon Nb/Mo-containing bainitic steels during high-temperature tempering, Mater Charact. 131 (2017) 298–305, https://doi.org/10.1016/j.matchar.2017.07.022.
[26] C.M. Enloe, F. D'Aiuto, H. Mohrbacher, Maximizing strengthening mechanisms in continuously annealed HSLA steel, Steel Properties and Applications in Conjunction with, Mater. Sci. Technol. 2021 (2021) 49–57, https://doi.org/10.33313/280/007.
[27] K. Zhu, O. Bouaziz, C. Oberbillig, M. Huang, An approach to define the effective lath size controlling yield strength of bainite, Mater. Sci. Eng. A 527 (2010) 6614–6619, https://doi.org/10.1016/j.msea.2010.06.061.
[28] E.V. Morales, R.A. Silva, I.S. Bott, S. Paciornik, Strengthening mechanisms in a pipeline microalloyed steel with a complex microstructure, Mater. Sci. Eng. A 585 (2013) 253–260, https://doi.org/10.1016/j.msea.2013.07.060.
[29] N. Kamikawa, K. Sato, G. Miyamoto, M. Murayama, N. Sekido, K. Tsuzaki, T. Furuhara, Stress-strain behavior of ferrite and bainite with nano-precipitation in low carbon steels, Acta Mater. 83 (2015) 383–396, https://doi.org/10.1016/j.actamat.2014.10.010.
[30] T. Gladman, Precipitation hardening in metals, Mater. Sci. Technol. 15 (1999) 30–36, https://doi.org/10.1179/026708399773002782.
[31] P. Xu, B. Bai, F. Yin, H. Fang, K. Nagai, Microstructure control and wear resistance of grain boundary allotriomorphic ferrite/granular bainite duplex steel, Mater. Sci. Eng. A 385 (2004) 65–73, https://doi.org/10.1016/j.msea.2004.04.073.
[32] R.M. Jentner, S.P. Tsai, A. Welle, S. Scholl, K. Srivastava, J.P. Best, C. Kirchlechner, G. Dehm, Automated classification of granular bainite and polygonal ferrite by electron backscatter diffraction verified through local structural and mechanical analyses, J Mater Res. (2023), https://doi.org/10.1557/s43578-023-01113-7.
[33] Y.W. Chen, Y.T. Tsai, P.Y. Tung, S.P. Tsai, C.Y. Chen, S.H. Wang, J.R. Yang, Phase quantification in low carbon Nb-Mo bearing steel by electron backscatter diffraction technique coupled with kernel average misorientation, Mater Charact. 139 (2018) 49–58, https://doi.org/10.1016/j.matchar.2018.01.041.
[34] E. Keehan, L. Karlsson, H.K.D.H. Bhadeshia, M. Thuvander, Electron backscattering diffraction study of coalesced bainite in high strength steel weld metals, Mater. Sci. Technol. 24 (2008) 1183–1188, https://doi.org/10.1179/174328407X226572.
[35] P. Cizek, The microstructure evolution and softening processes during high-temperature deformation of a 21Cr-10Ni-3Mo duplex stainless steel, Acta Mater. 106 (2016) 129–143, https://doi.org/10.1016/j.actamat.2016.01.012.
[36] G. Dehm, B.N. Jaya, R. Raghavan, C. Kirchlechner, Overview on micro- and nanomechanical testing: New insights in interface plasticity and fracture at small length scales, Acta Mater. 142 (2018) 248–282, https://doi.org/10.1016/j.actamat.2017.06.019.
[37] J.R. Greer, W.C. Oliver, W.D. Nix, Size dependence of mechanical properties of gold at the micron scale in the absence of strain gradients, Acta Mater. 53 (2005) 1821–1830, https://doi.org/10.1016/j.actamat.2004.12.031.
[38] R. Hosseinabadi, H. Riesch-Oppermann, J.P. Best, G. Dehm, C. Kirchlechner, Size scaling in bi-crystalline Cu micropillars containing a coherent twin boundary, Acta Mater. 230 (2022), 117841, https://doi.org/10.1016/j.actamat.2022.117841.
[39] E. Breitbarth, S. Zaefferer, F. Archie, M. Besel, D. Raabe, G. Requena, Evolution of dislocation patterns inside the plastic zone introduced by fatigue in an aged aluminium alloy AA2024-T3, Mater. Sci. Eng. A 718 (2018) 345–349, https://doi.org/10.1016/j.msea.2018.01.068.
[40] E.O. Hall, The Deformation and Ageing of Mild Steel: III Discussion of Results, Proc. Phys. Soc. London, Sect. B 64 (1951) 747–753, https://doi.org/10.1088/0370-1301/64/9/303.
[41] N.J. Petch, The cleavage strength of polycrystals, Journal of the Iron and Steel Institute. 174 (1953) 25–28.
[42] H. Bhadeshia, R. Honeycombe, Steels: microstructure and properties, Butterworth-Heinemann, 2017.
[43] J.R. Yang, C.Y. Huang, S.C. Wang, The development of ultra-low-carbon bainitic steels, Mater Des. 13 (1992) 335–338, https://doi.org/10.1016/0261-3069(92)90003-Z.
[44] S.C. Wang, R.I. Hsieh, H.Y. Liou, J.R. Yang, The effects of rolling processes on the microstructure and mechanical properties of ultralow carbon bainitic steels, Mater. Sci. Eng. A 157 (1992) 29–36, https://doi.org/10.1016/0921-5093(92)90095-I.
[45] M.R. Gilbert, S. Queyreau, J. Marian, Stress and temperature dependence of screw dislocation mobility in α-Fe by molecular dynamics, Phys Rev B Condens Matter Mater Phys. 84 (2011) 1–11, https://doi.org/10.1103/PhysRevB.84.174103.
[46] K.S. Ng, A.H.W. Ngan, Breakdown of Schmid's law in micropillars, Scr Mater. 59 (2008) 796–799, https://doi.org/10.1016/j.scriptamat.2008.06.019.
[47] G.I. Taylor, Plastic strain in metals, J. Inst. Metals. 62 (1938) 307–324.
[48] A. Sarkar, S. Sanyal, T.K. Bandyopadhyay, S. Mandal, Implications of microstructure, Taylor factor distribution and texture on tensile properties in a Ti-added Fe-Mn-Al-Si-C steel, Mater. Sci. Eng. A 767 (2019), 138402, https://doi.org/10.1016/j.msea.2019.138402.
[49] J.M. Rosenberg, H.R. Piehler, Calculation of the taylor factor and lattice rotations for bcc metals deforming by pencil glide, Metallurgical, Transactions 2 (1971) 257–259, https://doi.org/10.1007/BF02662666.
[50] B. Yang, C. Motz, M. Rester, G. Dehm, Yield stress influenced by the ratio of wire diameter to grain size - A competition between the effects of specimen microstructure and dimension in micro-sized polycrystalline copper wires, Phil. Mag. 92 (2012) 3243–3256, https://doi.org/10.1080/14786435.2012.693215.
[51] A.-P. Pierman, O. Bouaziz, T. Pardoen, P.J. Jacques, L. Brassart, The influence of microstructure and composition on the plastic behaviour of dual-phase steels, Acta Mater. 73 (2014) 298–311, https://doi.org/10.1016/j.actamat.2014.04.015.
[52] C.C. Tasan, M. Diehl, D. Yan, M. Bechtold, F. Roters, L. Schemmann, C. Zheng, N. Peranio, D. Ponge, M. Koyama, K. Tsuzaki, D. Raabe, An Overview of Dual-Phase Steels: Advances in Microstructure-Oriented Processing and Micromechanically Guided Design, Annu Rev Mater Res. 45 (2015) 391–431, https://doi.org/10.1146/annurev-matsci-070214-021103.
[53] H. Zhao, E.J. Palmiere, Influence of cooling rate on the grain-refining effect of austenite deformation in a HSLA steel, Mater Charact. 158 (2019), https://doi.org/10.1016/j.matchar.2019.109990.
[54] H. Zhao, B.P. Wynne, E.J. Palmiere, Effect of austenite grain size on the bainitic ferrite morphology and grain refinement of a pipeline steel after continuous cooling, Mater Charact. 123 (2017) 128–136, https://doi.org/10.1016/j.matchar.2016.11.025.
[55] M.K. Graf, H.-G. Hillenbrand, P. Peters, Accelerated cooling of plate for high-strength large-diameter pipe, The Metallurgical Society/AIME (1986) 165–179.
[56] D. Hull, D.J. Bacon, Introduction to dislocations, Elsevier, 2011.
[57] E. Orowan, Problems of plastic gliding, Proceedings of the Physical Society. 52 (1940) 8–22. https://doi.org/10.1088/0959-5309/52/1/303.
[58] D. Caillard, Kinetics of dislocations in pure Fe. Part I. In situ straining experiments at room temperature, Acta Mater. 58 (2010) 3493–3503, https://doi.org/10.1016/j.actamat.2010.02.023.
[59] D. Caillard, Kinetics of dislocations in pure Fe. Part II. In situ straining experiments at low temperature, Acta Mater. 58 (2010) 3504–3515, https://doi.org/10.1016/j.actamat.2010.02.024.
[60] A. Seeger, Peierls barriers, kinks, and flow stress: Recent progress, Zeitschrift Fuer Metallkunde/Materials Research and Advanced, Techniques 93 (2002) 760–777, https://doi.org/10.3139/146.020760.
[61] R. Gröger, V. Vitek, Breakdown of the schmid law in bcc molybdenum related to the effect of shear stress perpendicular to the slip direction, Mater. Sci. Forum 482 (2005) 123–126, https://doi.org/10.4028/0-87849-964-4.123.